

Learning to Sense Without ADCs: Exploiting Phasic Responses from Diffusive Memristors

Zhenhang Zhang
Syracuse University
zzhan281@syr.edu

Jingang Jin
Syracuse University
jjin24@syr.edu

Ruoyu Zhao
University of Southern California
rouyuz@usc.edu

Zixu Wang
University of Southern California
zixu@usc.edu

Tong Wang
University of Southern California
twang097@usc.edu

Rui Zuo
Syracuse University
rzu02@syr.edu

J. Joshua Yang
University of Southern California
jjoshuay@usc.edu

Qinru Qiu
Syracuse University
qinru.qiu@gmail.com

Abstract—This paper presents a neuromorphic system that integrates a low-cost, energy-efficient, and bio-realistic spike encoder with a spiking neural network (SNN). The two are jointly optimized via an online learning algorithm to enable temporal pattern detection across multi-channel sensor inputs. At the core of the system is a novel analog-to-spike converter based on diffusive memristors, which replaces conventional ADCs and provide a fundamentally different encoding scheme with substantially lower power consumption and reduced device footprint. However, the inherent variability of diffusive memristor devices introduces significant challenges for both frontend and backend design. To address this, we propose an Adaptive Gain Unit (AGU) and a frontend-backend co-adaptation strategy that supports real-time online learning updates of both the AGU and the classifier network. Experimental results on nine publicly available time-series datasets show that this adaptation improves accuracy by 4.19% on average. Furthermore, compared to conventional 8-bit ADCs and state-of-the-art level-crossing ADCs, the diffusive memristor-based system achieves comparable classification accuracy while offering orders of magnitude lower power consumption and improved area efficiency.

Index Terms—neuromorphic sensing, online adaptation, ADC-free, diffusive memristor.

I. INTRODUCTION

Dynamic information from the physical world is represented as temporal sequences, and the function of sensor systems is to detect patterns in these multi-channel time series. Traditional sensing systems rely on analog-to-digital converters (ADCs) to transform analog signals into the digital domain, where the digitized values within a fixed time window are buffered and processed for pattern classification. This approach introduces buffering delays and incurs significant power and cost overhead due to both the ADC and the required memory storage. Moreover, ADCs are often over-provisioned in terms of sampling frequency and data precision, leading to additional inefficiencies that further increase system complexity and energy consumption. Level-crossing ADCs (LC-ADCs) [1] offer an alternative to conventional uniform-sampling ADCs by recording signal values or generate output pulses only when

the input crosses predefined quantization levels, thereby reducing power consumption for signals with low activity. However, the buffering cost and latency remains and the variable output data rates complicates downstream digital processing.

A diffusive memristor (DMEM) is an emerging device characterized by volatile threshold-switching behavior arising from the diffusion and spontaneous relaxation of metallic filaments [2] [3]. This dynamic conductance modulation has been harnessed to emulate silicon-based nociceptors for biomedical sensing [4] and to reproduce leaky-integrate-and-fire membrane potentials in neuromorphic computing systems [5]. Its volatile nature, where the conductance rapidly increases in response to an input stimulus but then quickly relaxes back to the baseline once the stimulus is removed, closely resembles the behavior of a phasic receptor in biology, which responds strongly to changes but quiescent during sustained stimulation.

This property inspired us to design a 1M1C device as a hardware phasic receptor, enabling efficient encoding of transient events into sequence of spiking activities while naturally suppressing redundant steady-state information. The encoder offers benefits similar to those of an LC-ADC, significantly reducing data and power overhead by converting only meaningful temporal changes in the input into spikes. However, this is achieved with much simpler circuitry and substantially lower power consumption.

Three fundamental challenges remain in designing a neuromorphic sensing system with a DMEM-based analog-to-spike encoder. First, the sparsity of output spikes poses significant challenges for backend signal processing. Second, the complex nonlinear dynamics of a DMEM make its response sensitive not only to the amplitude of the input signal but also to its rate of change. A switching event occurs and an output spike is generated only when the input rises rapidly enough to exceed a dynamic threshold. This threshold is a temporal variable governed by the device's ion diffusion kinetics and hidden state, which are influenced by prior inputs and therefore difficult to predict in advance. While increasing the input voltage swing can raise the rate of change and promote switching, it may also unnecessarily increases output spiking activity, leading to higher power consumption. Finally, like all

This project was partially supported by NSF I/UCRC ASIC Center (CNS-1822165).

memristive devices, the DMEM exhibits significant variability. An input sequence that triggers high output activity in one encoder may fail to trigger any activity in another.

This work mitigates the above challenges by employing a spiking neural network (SNN) backend for spike-train classification and adopting a co-adaptation strategy that jointly optimizes both the device-specific input gain and the SNN classifier. Benefiting from its inherent recurrency, the SNN processes temporal sequences in a streaming fashion, thereby eliminating the need for input buffering. We further introduce an ADC-free, bio-realistic adaptive spiking encoder that integrates an *Adaptive Gain Unit (AGU)*, a DMEM and a capacitor. The AGU performs per-channel, trainable signal scaling, thereby mapping informative input ranges into the sensitive regime of the memristor encoder. The DMEM then carries out event-driven analog-to-spike conversion, functioning analogously to a biological phasic receptor. This design enables a compact silicon sensory neuron consuming orders of magnitude less power compared to conventional ADC-based frontend.

In biological systems, phasic receptors are commonly paired with tonic receptors, which provide continuous output in response to slow or sustained stimuli. Inspired by this principle, we also complement the DMEM based phasic receptor with a voltage comparator based tonic receptor to capture complementary aspects of sensory information. The following summarizes the contributions of this work:

- This work presents, to the best of our knowledge, for the first time, a compact, ADC-free, bio-inspired sensing frontend in which a diffusive memristor functions as a hardware phasic receptor to efficiently encode transient sensory events, complemented by a tonic receptor for sustained signals.
- We introduce a per-channel trainable AGU that, when combined with a frontend-backend co-adaptation scheme, simultaneously optimizes device-specific input gain and the spiking neural network (SNN) classifier.
- Our online learning algorithm, together with a surrogate gradient function, jointly trains the AGU and SNN to enable real-time adaptation to input signal characteristics, device variability, and task requirements.
- Experimental results show that the proposed neuromorphic sensing system achieves similar performance as conventional ANN classifier with 8-bit ADC, however, with orders of magnitude energy saving.

II. BACKGROUND AND RELATED WORKS

A. Neuromorphic Computing and Spike Encoders

Neuromorphic computing, and more specifically, spiking neural networks (SNNs), has gained growing attention for its potential in energy-efficient, bio-realistic computing. SNNs represent information through sequences of binary spiking activities. To convert analog input into spike trains, a well-crafted spike encoder should maintain the temporal and spatial characteristics of the input and map them sparsely into hyperdimensional vectors that are evenly distributed across the feature space for enhanced separation.

In [6], the authors showed that the intrinsic dynamics of a leaky-integrate-and-fire (LIF) neuron can be leveraged for analog to spike conversion. A follow up work [7] further proposed two spike encoder designs, population coding, which jointly encodes all channels of inputs using stateful neural networks. Recent hardware implementations of the spike encoder aim to build a stateful network using CMOS devices. Reference [8] proposed a CMOS based spike encoder using a delay-feedback-reservoir network. Each delay stage is implemented using a CMOS-based integrate-and-fire neuron comprising 11 transistors and a 120fF capacitor. LC-ADC [1] can also be used to convert analog input signals into spikes (or events) by sampling only when the input change crosses predefined voltage levels. Each crossing generates a digital spike that encodes the direction (upward or downward). However, compared to our single device encoder, their power consumption and area is still orders of magnitude higher.

B. Memristor Devices for Neuromorphic Computing

Memristors are two-terminal devices, generally composed of an insulating layer sandwiched between two conductive electrodes [9]. Their resistance is modulated by the history of the applied electrical stimulation. By varying the materials used for the insulating layers and electrodes, different types of memristors can be developed. In this work, two types of memristors, diffusive memristors (DMEM) and drift memristors are utilized. Both are filamentary-type memristors, with mobile ions moving under external stimulation to form conductive filaments inside the devices.

Drift memristor, characterized by their nonvolatile and controllable conductance changes, are commonly used to implement artificial synapses. Over the past few years, this type of memristor has matured significantly—transitioning from lab-scale fabrication to commercial foundry processes—resulting in high yield and reliable device characteristics suitable for large-scale deployment. Recent advancements in denoising technique has enabled individual drift memristors to reliably express thousands of distinct conductance states [10].

DMEMs are volatile memristors with the conductance decaying dynamically to the lowest level when there is no external stimulation. This behavior arises because the mobile ions in DMEM usually have low activation energies and high interfacial energies with the insulating material [2]. The low activation energies lead to the mobile ions moving dynamically inside the devices even without external stimulation. The high interfacial energy facilitates the break of the filament and the aggregation of mobile ions, resulting in spontaneous conductance decay. These two factors together determine the spontaneous decay speed of the diffusive memristor. The resistance of a diffusive memristor is a function of the length of its conduction channel x :

$$R_{\text{diffusive}} = R_{\text{on}} \cdot x + R_{\text{off}} \cdot \frac{e^{\frac{1-x}{\lambda}} - 1}{e^{\frac{1}{\lambda}} - 1} \quad (1)$$

where $x \in [0, 1]$ is the normalized variable representing conduction channel length, and λ is a constant characterizing

the tunneling barrier. $R_{\text{on}} = 1 \text{ M}\Omega$ and $R_{\text{off}} = 1 \text{ T}\Omega$ represent the ON and OFF state, respectively. When $x = 1$, conduction is fully ohmic; when $x = 0$, it is dominated by tunneling resistance.

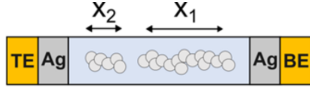


Fig. 1. The conduction channel of DMEM is further divided into two parts

As shown in Fig. 1, the conduction channel ($x \in [0, 1]$) of a diffusive memristor is further separated into two parts with different dynamics [11], $x = x_1 + x_2$, where the filament (x_1) and the residue (x_2) correspond to the fast-decaying relaxation and slow-decaying hidden memory respectively. The filament represents the thin and unstable portion of the channel with fast decaying, while the residue accounts for the thicker and relatively stable portion with slow decaying, which is converted from the filament via mobile ion aggregation. Their dynamics are governed by the following equations:

$$\frac{dx_1}{dt} = -\gamma_1 x_1 - \beta x_1 + \mu E \quad (2)$$

$$\frac{dx_2}{dt} = -\gamma_2 x_2 + \beta x_1 \quad (3)$$

where γ_1 and γ_2 are diffusion coefficients whose typical values are 600 and 2 respectively, β and μ are the filament-to-residue conversion rate and field-driven drift coefficient, whose typical values are 20 and 200 respectively. The electric field E across the device is estimated as:

$$E = \begin{cases} \frac{|V|}{\alpha + 1 - x}, & \text{if } x < 1 \\ |V|, & \text{if } x = 1 \end{cases} \quad (4)$$

where V is the voltage across the memristor, and $\alpha = 0.01$ is a constant characterizing the nonlinearity relation between E and x . When $x < 1$, the electric field mainly drops across the tunneling gap; when $x = 1$, it spans the fully formed conduction channel.

In this work, we leverage the complementary strengths of both device types. The drift memristor, with its high precision and tunable resistance states, is employed in the Adaptive Gain Unit (AGU) to dynamically scale the input signal. These scaling weights are updated in real-time using an online learning algorithm. Meanwhile, a diffusive memristor-based event-driven spike encoder is used to detect input signal variations, converting them into discrete current spikes based on the intrinsic leaky-integration properties of diffusive memristors. Together, this hybrid encoder architecture offers an efficient and compact alternative to traditional ADC.

C. Online Training of SNNs

Significant research is currently being conducted in the areas of online learning and continual learning [12] [13] [14] [15]. Because of the temporal filter behavior and internal memory, SNNs are sometimes viewed as a special type of Recurrent Neural Networks (RNN). From this perspective, it is a common practice to train SNNs using backpropagation through time (BPTT) method as a conventional RNN. However, BPTT

needs to unroll the recurrent structure on the whole sequence, hence usually requires memory and computation beyond what are available on edge devices. SOLSA [12] and OTTT [13] have introduced as Non-BPTT gradient-based optimization for SNNs. In this work, we use the SOLSA [12] learning, for each weight coefficient $w_{i,j}$ from with presynaptic neuron i and postsynaptic neuron j , SOLSA maintains a partial gradient $g_{i,j}[t]$ using the following equation:

$$g_{i,j}[t] = \sum_{t'=0}^t \mu_j[t'] \times \varepsilon_{i,j}[t'] \quad (5)$$

where $\mu_j[t]$ is the gradient of neuron j 's membrane potential backpropagated regardless of temporal dependencies, and $\varepsilon_{i,j}[t]$ is an accumulated trace signal on the ij th post synaptic potential (i.e., ij th input of the neuron after the dendritic filter) that accounts for the history. Our work extends the SOLSA learning algorithm, and apply it to train both the backend classifier and the AGU of the frontend encoder.

III. PROPOSED METHODOLOGY

A. Overall Framework of the Adaptive Spiking Encoder

Our goal is to replace power-hungry, discretely quantized ADC with a neuromorphic frontend that co-trains with a backend SNN for sensory applications. Fig. 2 depicts the block diagram of the overall system.

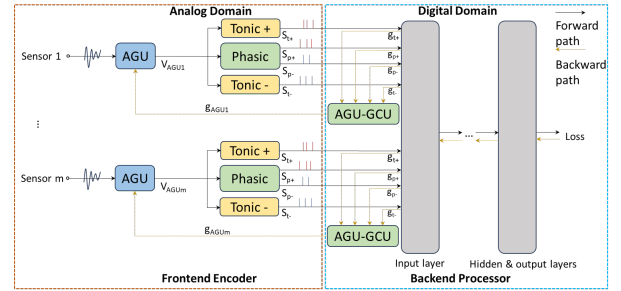


Fig. 2. Overall architecture of the proposed ADC-free neuromorphic sensing system. Each input channel is first scaled by a trainable Adaptive Gain Unit (AGU), then converted into event-driven spikes by a diffusive memristor (phasic receptor) complemented by comparator based skip connections (tonic receptor), and finally processed by a backend SNN with joint adaptation.

Without loss of generality, we assume that each channel of the sensor input is a voltage signal, v_{in} , normalized to a fixed range (e.g. $[-1, 1]$). The input signal of the i -th channel is scaled by an adaptive gain unit (AGU) with controllable gain to generate the scaled voltage y_i , $y_i = w_i v_{in}[i]$. The amplifier gain, w_i , is optimized and controlled by the backend processor during the training process. To ensure safe and energy efficient operation, the gain w_i is limited to the range $[-2, 2]$ such that the output voltage y_i is within $\pm 2V$. Implementation details of AGU will be discussed in III-B.

The amplified voltage y_i drives a 1M1C device whose drift-diffusion dynamics produce sparse, temporally encoded dual-channel spikes for positive and negative events similar to the role of a phasic receptor in neuromorphic systems. To complement this, skip connections are incorporated to provide

level based output similar to tonic receptors. Details of the encoder are provided in III-C.

The output of the encoders are spike trains reshaped into digital pulses and processed by backend processor in digital domain. The processor further supports in-place gradient calculation and weight update for both the AGU and the SNN, thereby enabling co-adaptation between the frontend and backend. Details of the training methods can be found in III-D.

B. Adaptive Gain Unit (AGU)

Traditional analog amplifiers only amplify the signals with a fixed ratio, and cannot adapt to different types of sensory inputs with different ranges. To overcome this limitation, we introduce a self-adaptive amplifier using drift memristor-based circuits, leveraging their highly tunable resistance states.

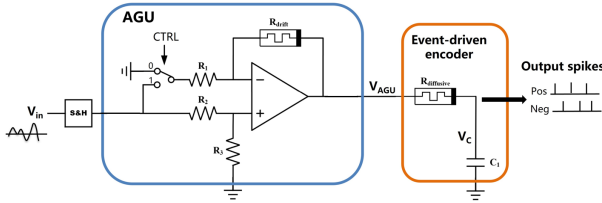


Fig. 3. System front end with an Adaptive Gain Unit (AGU) followed by a diffusive-memristor encoder. Inputs are normalized to ± 1 V; the AGU scales each channel with a trainable gain in $[-2, 2]$.

The circuit model of the AGU is shown in Fig. 3. By adjusting the resistance of the drift memristor (R_{drift}) and the control signal (CTRL), both the positive and negative amplification factors can be achieved. Specifically, when CTRL is set to 1, R_1 is directly connected to the input signal V_{in} , and the gain of the AGU is:

$$A_v = \frac{V_{\text{AGU}}}{V_{\text{in}}} = \frac{1}{2} - \frac{R_{\text{drift}}}{2R_1} \quad (6)$$

When CTRL is set to 0, R_2 is connected to ground, and the AGU delivers the corresponding voltage gain of:

$$A_v = \frac{V_{\text{AGU}}}{V_{\text{in}}} = \frac{1}{2} + \frac{2R_{\text{drift}}}{R_1} \quad (7)$$

where, R_1 and R_2 are 9 k Ω , and R_3 is 1 k Ω , and the resistance of the drift memristor (R_{drift}) is tunable, ranging from 1 k Ω to 20 k Ω . By properly adjusting R_{drift} and CTRL, the amplification factor (A_v) can be dynamically adjusted in the range of $[-2, 2]$, enabling both positive and negative gain modulation.

Fig. 4 shows waveforms from Cadence Spectre simulation in which the adaptive spiking encoder processes a sample signal extracted from the Epilepsy dataset. After sampling, the input signal is first fed into the AGU. The green line in the first row represents the signal after the sample-and-hold (S/H) operation, while the green line denotes the AGU output signal V_{AGU} . The sampling frequency is 1 kHz. In this simulation, the amplifier gain was set to 2 based on the training result. To achieve this, the resistance of the drift memristor was configured to 6.75 k Ω , and CTRL was set to 0. This adaptive amplification improves the sensitivity of the spiking encoder, making it more responsive to subtle variations in the input and

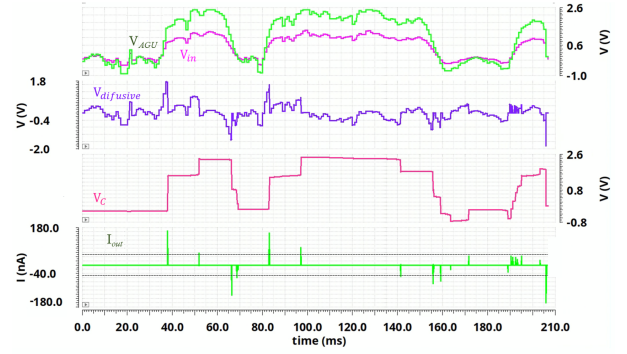


Fig. 4. Circuit simulation result of the Adaptive Spiking Encoder.

enhancing the possibility of spike generated by the diffusive memristor based encoder.

C. Spike encoder

As shown in Fig. 3, the output of the AGU drives a spike encoder consisting of a diffusive memristor in series with a capacitor, whose dynamics are governed by Equations (1)-(4). When the conduction channel is formed and the diffusive memristor enters the "on" state, it charges the capacitor and generate a current spike. If the current exceeds a defined threshold, a digital spike is generated. In our experiment, this threshold is set to be 50 nA.

As the capacitor becomes fully charged, the voltage across the diffusive memristor drops to zero, causing both the filament and residue states to decay over the remainder of the sampling interval. In the subsequent interval, if the input voltage differs from the capacitor voltage, an electric field is re-established, driving the filament and residue states to grow again. The growth rate, governed by the magnitude of the electric field, determines when the next current spike occurs. Depending on the polarity of the voltage across the diffusive memristor, the resulting current spike may be either positive or negative. We denote positive and negative spikes as S_{p+} and S_{p-} respectively.

The diffusive memristor in our system acts as a phasic receptor, responding primarily to changes in the input signal with transient current spikes. While this is excellent for detecting novelty, a complete biological sensing system also requires tonic receptors to provide sustained responses, conveying information about the continuous presence or magnitude of a stimulus. Following [7], dual channel skip connections are introduced as tonic receptors:

$$S_{t+} = H(V_{\text{AGU}} - V_{\text{th}}), \quad S_{t-} = H(-V_{\text{AGU}} - V_{\text{th}}), \quad (8)$$

where $V_{\text{th}} = 1$ V, and $H()$ is the Heaviside function. Together with the encoder's positive/negative events $\{S_{p+}, S_{p-}\}$, each sensor channel yields four binary outputs $\mathcal{S} = \{S_{t+}, S_{t-}, S_{p+}, S_{p-}\}$, which preserve both polarities at low latency and raise the effective event rate available to the backend under low voltage.

D. SNN Model and Customized Gradient Updates

The backend SNN classifier is constructed from leaky integrate-and-fire (LIF) neurons with post-synaptic potentials (PSPs) [16]. The PSP, denoted as $F[t]$, represents the output of a filter located at each synapse. To simplify the design, a first order IIR filter is adopted. For the i th input, the PSP is updated using the following equation:

$$F_i[t] = \alpha F_i[t-1] + \beta I_i[t], \quad (9)$$

where $I_i[t]$ is the i th input of the neuron. The membrane potential $V[t]$ of the neuron then evolves according to the following dynamics:

$$V[t] = \lambda V[t-1] + \sum_i F_i[t] + \xi V_{th} O[t-1], \quad (10)$$

where V_{th} is the threshold voltage and ξ is a coefficient controls reset process, It is set to 0.5 in our system. $O[t-1]$ is the output of this neuron at time $t-1$, where

$$O[t-1] = H(V[t-1] - V_{th}).$$

The backend classifier is trained online with SOLSA [17], while the AGU gains $\{A_v(i)\}$ are co-optimized. Let the four front-end outputs per channel be $\mathcal{S} = \{S_{t+}, S_{t-}, S_{p+}, S_{p-}\}$, and denote by g_{\bullet} the upper stream gradients backpropagated (via SOLSA) to each channel of the input layer. We calculate ΔA_v in each time step using a purely digital, event-driven rule:

$$\Delta A_v \propto g_{t+} S_{t+} + g_{t-} S_{t-} + g_{p+} S_{p+} + g_{p-} S_{p-}. \quad (11)$$

A stream contributes gradient only when it emits an event; otherwise its contribution is zero. This *event-gated gradient* rule eliminates surrogate derivatives, aligns with the device's event-driven nature, and avoids unnecessary computation when no events are present. As in SOLSA, weight changes are accumulated over time and applied at sparse update points. The A_v is clipped to the range of $[-2, 2]$ and rounded to 8-bit quantization of the drift memristor.

IV. EXPERIMENTS AND RESULTS

A. Experimental Setup and Datasets

To evaluate the effectiveness of the proposed adaptive spiking encoder, we developed a behavioral simulator of the sensing platform, which includes the AGU, an ODE-based behavioral model for the spike encoder, and the backend classifier and learning algorithm. The behavioral model of the diffusive memristor as shown in Equations (1)-(4) is adopted from [11]. The simulation operates at mixed time resolutions: we use a $1\mu s$ time resolution for the analog simulation, while the digital system is simulated with a time step of $1ms$. The drift memristor in the AGU can be programmed into 256 levels ranging from $1k\Omega$ to $20k\Omega$. Power is obtained from behavioral simulations of the ODE-based memristor model, while Fig. 4 provides circuit-level Spectre validation.

We validate our method on nine publicly available time-series classification datasets from the UCR/UEA Repository [18], including Japanese Vowels [19]. These datasets encompass biomedical, motion, and speech signals, making them ideal for evaluating the encoder's adaptability across different

domains. Their information is summarized in Table ???. We assume that sample and hold were used at the input with 1 KHz frequency. Power consumption scales approximately linearly with bandwidth; all reported numbers are normalized to 1 kHz for fairness

B. Accuracy Comparison with Baselines

Table I reports classification accuracy across nine datasets, providing a comparison between SNN and ANN based systems. The SNN based systems uses either memristor or LC-ADC based spike encoder, and are denoted as *MEM* and *LCE* respectively. Each system has been configured either with or without AGU, denoted as $\{MEM, LCE\}+$ and $\{MEM, LCE\}-$ respectively. Both SNNs and AGUs are trained to adapt to the input. The SNN has three fully connected layers built with LIF neurons with PSP as explained in Section III.D. Besides the input and output layers, the two hidden layers have 100 neurons each. The two ANN based systems use 8-bit ADC to convert input from analog to digital and they use either MLP or LSTM models for classification. To ensure a fair comparison, the LSTM has 50 hidden units, such that it has similar number of trainable parameters as the SNN. The MLP model assumes that the entire input sequence is buffered and classified at the same time. Hence it has a huge input layer. It also has two hidden layers. Their size varies from 1,000 to 4,000 neurons depend on the size of the input layer. The MLP model is evaluated here as a baseline to show that the classification problem is non-trivial.

Table I also reports the percentage accuracy improvements of all the baselines over the proposed memristor with AGU system (i.e., MEM+). In addition, it presents the average spiking rate (Rate) and power consumption per channel for diffusive memristor and LC-ADC based encoder. The power consumption for LC-ADC is estimated using a model derived from data presented in [1]. Based on the reference, the LC-ADC has $16nW$ static power consumption and an energy dissipation of $2.05pJ$ per spike. The power consumption for diffusive memristor was measured from simulation. Unlike the LC-ADC, the diffusive memristor-based spike encoder does not have static power consumption. The energy is only dissipated in charging or discharging the capacitor. The reported energy counted all current activities, including those small glitches that are lower than $50nA$ and consequently didn't trigger any spike generation. For both systems, the power consumption of AGU is not included. The power consumption of 8-bit ADC is not reported in the table, however, it is usually in the μW to mW range when operating at $1KHz$.

Several important observations can be made from the table. First, adding the AGU improves accuracy for both LCE and MEM across all datasets, confirming the benefit of per-channel adaptive scaling that maps informative signal ranges into the sensitive operating region of the encoder.

Second, memristor-based and LC-ADC based systems achieve very similar accuracy. Their average difference is only 0.67%. This is expected as their operation mechanisms are similar. However, the proposed MEM+ encoder offers

TABLE I

ACCURACY COMPARISON ACROSS ENCODERS AND DIGITAL BASELINES. “-” DENOTES SYSTEMS WITHOUT AGU, “+” DENOTES SYSTEMS WITH AGU. Δ COLUMNS REPORT RELATIVE CHANGE VS. MEM+, AND THE LAST TWO COLUMNS REPORTS SPIKING RATE.

Dataset	MEM+		MEM-		LCE-		LCE+		MLP		LSTM		Power (nW)		Spikes MEM+	Spikes LCE+
	ACC	ACC	Δ (%)	ACC	Δ (%)	ACC	Δ (%)	ACC	Δ (%)	ACC	Δ (%)	MEM+	LCE+			
RacketSports	0.828	0.782	-5.56	0.782	-5.56	0.835	+0.85	0.816	-1.45	0.917	+10.75	1.140	16.00143	0.061	0.116	
Epilepsy	0.985	0.978	-0.71	0.920	-6.60	0.956	-2.95	0.610	-38.07	0.962	-2.34	1.270	16.00165	0.098	0.269	
EMG_Action	0.906	0.765	-15.54	0.771	-14.95	0.845	-6.73	0.282	-68.87	0.910	+0.44	1.029	16.00262	0.076	0.160	
FingerMovement	0.630	0.580	-7.94	0.600	-4.76	0.610	-3.17	0.510	-19.05	0.580	-7.94	0.389	16.01188	0.074	0.207	
BasicMotion	1.000	1.000	+0.00	1.000	+0.00	1.000	+0.00	0.975	-2.50	1.000	+0.00	0.825	16.00150	0.072	0.122	
Jap. Vowels	0.924	0.916	-0.87	0.916	-0.87	0.918	-0.65	0.965	+4.44	0.958	+3.68	0.811	16.00684	0.108	0.278	
Self Reg	0.881	0.850	-3.52	0.839	-4.77	0.897	+1.81	0.891	+1.14	0.874	-0.79	0.027	16.00263	0.044	0.214	
A.W.R.	0.930	0.916	-1.51	0.863	-7.20	0.933	+0.32	0.980	+5.38	0.963	+3.55	0.262	16.00524	0.106	0.284	
SpokenArabic	0.915	0.909	-0.66	0.916	+0.11	0.926	+1.20	0.725	-20.77	0.978	+6.89	0.720	16.00637	0.104	0.239	
Average Δ	-	-	-4.19	-	-4.83	-	-0.67	-	-15.35	-	+1.59	-	16.00446	-	-	

TABLE II
DATASET INFORMATION

Dataset	# Input	Seq. Len.	# Classes	Task
RacketSports [18]	6	30	4	Motion
BasicMotion [18]	6	100	4	Motion
EMG_Action [20]	8	1000	10	Motion
Epilepsy [21]	3	207	4	Biomedical
FingerMovement [22]	28	50	2	Biomedical
SelfReg [23]	6	896	2	Biomedical
Jap. Vowels [19]	12	29	9	Speech
A.W.R. [24]	9	144	25	Speech
SpokenArabic [25]	13	40	10	Speech

substantial advantages in terms of energy efficiency. The diffusive memristor consumes only 0.02–1.27 nW per channel on average, whereas LC-ADC is dominated by its static power consumption which is $10X$ greater than the power consumption of memristor. In addition, we found that MEM generates significantly fewer spikes. Its spiking rate is more than $2X$ lower than that of LC-ADC. The lower spiking activity directly reduces transmission and synaptic processing cost in the backend SNN, yielding both device-level and system-level efficiency gains.

Third, the LSTM based classifier, in average, only has 1.5% higher accuracy compared to MEM+, which shows that the spike encoder effectively preserves the temporal information of the input. And finally, the simple MLP model performs poorly compared to all other models, which confirms that the classification is not a trivial task.

Taken together, these results demonstrate that the proposed MEM+AGU encoder achieves accuracy on par with conventional 8-bit ADC-based system while providing a more bio-realistic, device-native alternative to ADC.

C. Robustness under Device Variations

Table I is obtained under the assumption that all encoders are identical and stable. Next, we evaluate the MEM+ systems in the presence of device-to-device (d2d) and cycle-to-cycle (c2c) variations. Specifically, we assume that the diffusion coefficients of filament and residual states (γ_1 and γ_2 respectively) follow a normal distribution with 30% coefficient of variation. Under d2d variation, each DMEM device is randomly sampled at initialization and operates consistently throughout training and testing. Under c2c variation, new values of γ_1 and γ_2 are sampled from the distribution at every time step. Each experiment is repeated 3 times and we report the mean, minimum and maximum results.

TABLE III
ACCURACY OF MEM+ UNDER DEVICE-TO-DEVICE (D2D) AND CYCLE-TO-CYCLE (C2C) VARIATIONS.

Dataset	d2d	Adpt	c2c	Adpt	Ideal	d2d	NoAdpt	c2c	NoAdpt
RacketSports	0.811±0.010	0.801±0.004	0.828	0.721 ± 0.088	0.697 ± 0.092				
Epilepsy	0.987±0.004	0.987±0.008	0.985	0.974 ± 0.022	0.987 ± 0.004				
EMG_Action	0.852±0.015	0.878±0.012	0.906	0.817 ± 0.045	0.837 ± 0.037				
FingerMovement	0.627±0.032	0.623±0.021	0.630	0.570 ± 0.070	0.530 ± 0.087				
BasicMotion	0.975±0.025	0.975±0.025	1.000	0.683 ± 0.274	0.717 ± 0.245				
Jap. Vowels	0.910±0.009	0.912±0.006	0.924	0.864 ± 0.038	0.862 ± 0.049				
Self Reg	0.874±0.007	0.877±0.009	0.881	0.832 ± 0.043	0.828 ± 0.049				
A.W.R.	0.903±0.003	0.909±0.007	0.930	0.818 ± 0.079	0.856 ± 0.043				
SpokenArabic	0.919±0.005	0.914±0.004	0.915	0.867 ± 0.040	0.850 ± 0.057				

Table III reports the accuracy of MEM+ system under d2d and c2c variations. For comparison, we also report the accuracy from MEM systems without adaptation as well as from the ideal MEM+ system where all encoders are assumed identical and consistent.

As shown in the table, with adaptation, both d2d and c2c variations have only marginal impact on system performance. Compared to the ideal case, the average accuracy degradation across the 9 datasets is only 1.7% and 1.5% respectively. The system is slightly more robust to the c2c variation likely because the output activity of the DMEM is determined by the accumulated effect of the diffusion process. Since the variation is unbiased, its accumulated influence remains low. In contrast, without adaptation, both d2d and c2c variations reduce the average system accuracy by 12.9% and 12.8% in average respectively across the nine datasets. More importantly, adaptation significantly reduces performance variability across systems: deviations in accuracy are reduced on average by 81% under d2d variation and 64% under c2c variation.

V. CONCLUSION

This work presents a hardware-integrated, bio-realistic, and trainable spike encoder system co-designed with a spiking neural network. By leveraging a DRMEM-based AGU and a DMEM-based spike encoder, the proposed architecture eliminates the need for conventional ADCs and enables efficient analog-to-spike conversion without discrete-level quantization. Furthermore, a frontend–backend co-training algorithm is developed to enhance system performance, facilitate deployment, and to adapt effectively to device-to-device and cycle-to-cycle variations. Reported results are based on behavioral-level with circuit-level simulation. Our future work will extend the framework toward hardware prototyping and broader evaluation.

REFERENCES

- [1] J. Chen, H. Wu, J. Yang, and M. Sawan, "A 97 fJ/conversion neuron-ADC with reconfigurable sampling and static power reduction," *arXiv preprint arXiv:2211.15319*, 2022. [Online]. Available: <https://arxiv.org/abs/2211.15319>
- [2] R. Zhao *et al.*, "Memristive ion dynamics to enable bio-realistic computing," *Chemical Reviews*, vol. 125, no. 2, pp. 745–785, 2024.
- [3] R. Midya, Z. Wang, J. Zhang, S. E. Savel'ev, C. Li, M. Rao, M. H. Jang, S. Joshi, H. Jiang, P. Lin, K. Norris, N. Ge, Q. Wu, M. Barnell, Z. Li, H. L. Xin, R. S. Williams, Q. Xia, and J. J. Yang, "Anatomy of ag/hafnia-based selectors with 10^{10} nonlinearity," *Advanced Materials*, vol. 29, no. 12, p. 1604457, Mar. 2017.
- [4] J. Yoon, Z. Wang, K. Kim *et al.*, "An artificial nociceptor based on a diffusive memristor," *Nature Communications*, vol. 9, p. 417, 2018.
- [5] Z. Wang, S. Joshi, S. Savel'ev *et al.*, "Fully memristive neural networks for pattern classification with unsupervised learning," *Nature Electronics*, vol. 1, pp. 137–145, 2018.
- [6] H. Fang *et al.*, "Encoding, model, and architecture: Systematic optimization for spiking neural network in FPGAs," in *Proceedings of the 39th International Conference on Computer-Aided Design (ICCAD)*, 2020.
- [7] J. Jin, Z. Zhang *et al.*, "Exploring spike encoder designs for near-sensor edge computing," in *Proceedings of the Neuro Inspired Computational Elements Conference (NICE)*, 2025.
- [8] C. Zhao, J. Li, and Y. Yi, "Making neural encoding robust and energy efficient: An advanced analog temporal encoder for brain-inspired computing systems," in *Proceedings of the IEEE/ACM International Conference on Computer-Aided Design (ICCAD)*. IEEE, 2016.
- [9] J. J. Yang *et al.*, "Memristive switching mechanism for metal/oxide/metal nanodevices," *Nature Nanotechnology*, vol. 3, no. 7, pp. 429–433, 2008.
- [10] M. Rao *et al.*, "Thousands of conductance levels in memristors integrated on CMOS," *Nature*, vol. 615, no. 7954, pp. 823–829, 2023.
- [11] Y. Zhuo *et al.*, "A dynamical compact model of diffusive and drift memristors for neuromorphic computing," *Advanced Electronic Materials*, vol. 8, no. 8, p. 2100696, 2022.
- [12] Z. Zhang, J. Jin, Q. Qiu *et al.*, "SOLSA: Neuromorphic spatiotemporal online learning for synaptic adaptation," in *Proceedings of the 29th Asia and South Pacific Design Automation Conference (ASP-DAC)*. IEEE, 2024.
- [13] M. Xiao *et al.*, "Online training through time for spiking neural networks," in *Advances in Neural Information Processing Systems (NeurIPS)*, vol. 35, 2022, pp. 20717–20730.
- [14] Y. Ma *et al.*, "LVP-CLIP: Revisiting CLIP for continual learning with label vector pool," in *Proceedings of the IEEE/CVF Conference on Computer Vision and Pattern Recognition (CVPR)*, 2025.
- [15] A. Shrestha *et al.*, "In-hardware learning of multilayer spiking neural networks on a neuromorphic processor," in *Proceedings of the 58th ACM/IEEE Design Automation Conference (DAC)*. IEEE, 2021.
- [16] H. Fang, A. Shrestha, Z. Zhao, and Q. Qiu, "Exploiting neuron and synapse filter dynamics in spatial temporal learning of deep spiking neural network," in *Proceedings of the 29th International Joint Conference on Artificial Intelligence (IJCAI)*. International Joint Conferences on Artificial Intelligence Organization, 2020, pp. 2799–2806.
- [17] Z. Zhang, J. Jin, H. Fang, and Q. Qiu, "SOLSA: Neuromorphic spatiotemporal online learning for synaptic adaptation," in *Proceedings of the 29th Asia and South Pacific Design Automation Conference (ASP-DAC)*. IEEE, 2024, pp. 848–853.
- [18] A. Bagnall, H. A. Dau, J. Lines, M. Flynn, J. Large, A. Bostrom, P. Southam, and E. Keogh, "The uea multivariate time series classification archive, 2018," *arXiv preprint arXiv:1811.00075*, 2018, accessed: Sep. 14, 2025. [Online]. Available: <http://www.timeseriesclassification.com>
- [19] M. Kudo, J. Toyama, and M. Shimbo, "Japanese vowels," 1999, accessed: Sep. 14, 2025. [Online]. Available: <https://doi.org/10.24432/C5NS47>
- [20] T. Theodoridis, "Emg physical action data set," UCI Machine Learning Repository, 2011, accessed: Sep. 14, 2025. [Online]. Available: <https://doi.org/10.24432/C53W49>
- [21] J. Villar, P. Vergara, M. Menéndez, E. de la Cal, V. González, and J. Sedano, "Generalized models for the classification of abnormal movements in daily life and its applicability to epilepsy convulsion recognition," *International Journal of Neural Systems*, vol. 26, no. 6, p. 1650037, 2016.
- [22] B. Blankertz, G. Curio, and K.-R. Müller, "Classifying single trial eeg: Towards brain computer interfacing," in *Advances in Neural Information Processing Systems (NeurIPS)*, vol. 14. Cambridge, MA, USA: MIT Press, 2001, pp. 157–164.
- [23] N. Birbaumer, N. Ghanayim, T. Hinterberger *et al.*, "A spelling device for the paralysed," *Nature*, vol. 398, pp. 297–298, 1999.
- [24] "Articulatory word recognition," UEA & UCR Time Series Classification Repository, 2018, accessed: Sep. 14, 2025. [Online]. Available: <https://www.timeseriesclassification.com/dataset.php>
- [25] M. Bedda and N. Hammami, "Spoken arabic digit [dataset]," UCI Machine Learning Repository, 2008, accessed: Sep. 14, 2025. [Online]. Available: <https://doi.org/10.24432/C52C9Q>